metals

MDPI

Article

Dealloying of Cu-Mg-Ca Alloys

Wael Ben Mbarek [1], Eloi Pineda [2,*], Lluïsa Escoda [3], Joan Josep Suñol [3] and Mohamed Khitouni [1]

1 Laboratoire de Chimie Inorganique, Faculté des Sciences, Université de Sfax, Ur-11-Es-73, Sfax 3029, Tunisia; benmbarek.wael@hotmail.fr (W.B.M.); khitouni@yahoo.fr (M.K.)
2 Departament de Física, Centre de Recerca en Ciència i Enginyeria Multiescala de Barcelona, Universitat Politècnica de Catalunya-BarcelonaTech, 08019 Barcelona, Catalonia, Spain
3 Departament de Física, Universitat de Girona, 17071 Girona, Catalonia, Spain; lluisa.escoda@udg.edu (L.E.); joanjosep.sunyol@udg.edu (J.J.S.)
* Correspondence: eloi.pineda@upc.edu; Tel.: +34-935-521-141

Received: 18 October 2018; Accepted: 6 November 2018; Published: 8 November 2018

Abstract: The chemical dealloying of Cu-Mg-Ca alloys in free corrosion conditions was investigated for different alloy compositions and different leaching solutions. For some of the precursor alloys, a continuous, pure fcc copper with nanoporous structure can be obtained by dealloying in 0.04 M H_2SO_4 solution. Superficial nanoporous copper structures with extremely fine porous size were also obtained by dealloying in pure water and 0.1 M NaOH solutions. The dealloying of both amorphous and partially crystalline alloys was investigated obtaining bi-phase nanoporous/crystal composites with microstructures depending on the precursor alloy state. The fast dissolution of Mg and Ca makes the Cu-Mg-Ca system an ideal candidate for obtaining nanoporous copper structures with different properties as a function of different factors such as the alloy composition, the quenching process, and leaching conditions.

Keywords: amorphous materials; metallic glasses; biocompatible materials; corrosion; nanoporous copper

1. Introduction

Chemical dealloying was classically used to create nobler surfaces on metallic materials, thus improving the anticorrosion or aesthetic properties of the bulk alloy. Despite being a traditional technique used by metallurgists and goldsmiths for centuries, the atomistic understanding of the dealloying process, as well as the factors controlling the size of porous and ligaments that may appear on the leached surface, have only been revealed by modern nanoscale characterization and simulation techniques [1,2]. These factors are namely the bulk and surface diffusivity of the alloy components, the dissolution kinetics at the metal/electrolyte contact layer and the diffusivity in the electrolyte solution.

The nanoporosity produced by dealloying can be detrimental for some mechanical properties, as it increases brittleness and may facilitate crazing and crack propagation but can be beneficial for some functional properties. The increase of specific surface combined with electrical conductivity makes metallic nanoporous structures useful in a wide range of applications such as biological and chemical sensing, catalysis or advanced materials for battery electrodes [3–7], just to name a few. Furthermore, these metallic nanostructures may show low global density, nano-channel interconnectivity and even good merit indices for some mechanical functions [8,9] that open the possibility to design new technologies in the fields of micro-mechanics [8] and micro-fluidics [10].

Nanoporous metals such as gold, silver, platinum, palladium and copper have been synthesized by a large variety of chemical and physical methods [11,12]. Among them, chemical and electrochemical

dealloying is able to produce three-dimensional nanoporous metals with open pores of size controlled by the alloy composition, electrolyte type and concentration, potential of the electrochemical cell, temperature and dealloying time [2,13]. This method has been successfully implemented in the manufacture of noble nanoporous metals from different kinds of precursor alloys with binary and ternary compositions, such as Pt-Cu [14], Au-Ag [15] and Ag-Au-Pt [16].

In comparison with more noble metals, nanoporous copper (np-Cu) is an attractive, more inexpensive material with excellent perspectives for wide application in both laboratories and industry [4,17]. Np-Cu has been synthesized by dealloying various intermetallic, crystalline compounds such as Cu-Mn [4,18], Cu-Al [13], Cu-Zr [19] and Cu-Mg [20] alloys. To obtain np-Cu with ideal three-dimensional, bicontinuous structure it is necessary a single-phase solid solution as a precursor alloy. However, the concentration ranges of homogeneous solid solutions are limited in crystalline phases as defined by the corresponding phase diagrams. On the other hand, amorphous metals or metallic glasses (MG) have wider solubility ranges inherited from the liquid phase. Therefore, MGs have the advantage of higher chemical homogeneity down to the nanometer scale combined with a much wider compositional range than crystalline alloys. Currently, thousands of MG have been reported in various alloy systems, thus offering abundant candidates for manufacturing nanoporous metals. Some examples of fabrication of np-Metal from metallic glass precursors are the electrochemical dealloying of $Pd_{30}Ni_{50}P_{20}$ in 1 M sulfuric acid obtaining np-Pd(Ni) [21], np-Au and np-Au(Pd) structures obtained by electrochemical deallyoing of $Au_{35}Si_{20}Cu_{28}Ag_7Pd_5Co_5$ and $Au_{30}Si_{20}Cu_{33}Ag_7Pd_{10}$ in 1 M sulfuric acid [21,22] and np-Cu obtained by free corrosion of $Mg_{60}Cu_{30}Y_{10}$ and $Mg_{50}Cu_{40}Y_{10}$ glasses in 0.04 M H_2SO_4 solutions [23,24].

The presence of easy dissolving elements, with large and negative corrosion potentials, combined with nobler species with positive potentials is expected to facilitate the leaching process. In some cases, it is even not necessary the application of an external potential to promote the formation of the np-Metallic structure. Therefore, MG with Ca and Mg contents provide good candidates for np-Metal precursors, as these two elements are easily dissolved in acidic aqueous solutions or even when submerged in simple water [25]. Fortunately, there is a wide range of binary and ternary (Mg, Ca)-(Ag, Al, Cu, Ni, Zn) glass-forming compositions [26–29]. Indeed, the rapid dissolution of Mg in free corrosion conditions was reported in the above mentioned works using Cu-Mg-Y amorphous precursors [23,24]. Also pure np-Ag was obtained from Ag-Mg-Ca glassy alloys by electrochemical dealloying using $MgCl_2$ [30] and low concentrated HCl aqueous solutions as electrolytes [31]. The ligament and pore size was tuned by applying different conditions of electrolyte concentration and temperature.

Furthermore, (Mg, Ca)-based alloys are good candidates for some biomedical applications such as biocompatible resorbable implants [32,33]. The corrosion behavior can be modified depending on the composition and microstructure; amorphous phases were reported to be slightly more corrosion resistant that their crystalline counterparts [32]. Investigation of the corrosion behavior of these alloys is therefore needed to choose which compositions may be the better candidates to be probed in biocompatible applications.

The aim of this work is to assess the dealloying process of Cu-Mg-Ca alloys. This alloy system has some peculiarities; it shows glass-forming ability (GFA) for some compositions and combines Cu with easily dissolving and environmentally friendly elements such as Ca and Mg. The production of np-Cu from Cu-Mg-Ca was never reported before. In the following sections we present the results obtained for various compositions, with different degrees of crystallinity, and leached in different solutions.

2. Materials and Methods

Metallic glass ribbons of Cu-Mg-Ca were produced by melt-spinning method. The ribbons obtained were 20–40 μm thick and 1–3 mm wide. Dealloying of the melt-spun ribbons was conducted by direct corrosion immersing pieces of ribbons in different solutions, namely, pure distilled water (pH = 7), 1 M HCl (pH = 3), 0.1 M NaOH (pH = 10) and 0.04 M H_2SO_4. All dealloying processes were

performed at room temperature. After dealloying, the as-dealloyed samples were rinsed with distilled water and dehydrated alcohol and kept in a vacuum chamber to avoid oxidation. The morphology and structure were examined using scanning electron microscopy (SEM) and energy-dispersive X-ray spectroscopy (EDS) in a Zeiss Neon40 (Zeiss, Jena, Germany) apparatus. Characterization of the interior of the ribbons was performed by in situ cutting a trench of approximately 15 μm depth, thus arriving to the center of the ribbons thickness. The trench was dug by Focused Ion Beam of Ga ions after depositing a Pt protective coating. X-ray diffraction (XRD) of as-quenched and dealloyed ribbons was performed on a Siemens D500 (Siemens, Munich, Germany) using CuKα radiation, phase identification was performed by means of X'pert High Score Plus software (PANalytical, version 2.0.1, Almelo, The Netherlands). The size distribution of the pore size was obtained from the SEM images by ImageJ (version 1.51j8, National Institutes of Health, Bethesda, MD, USA) software analysis; erode and de-speckle algorithms were applied to isolate the pore images from the background and the remaining touching particles were removed manually prior to the calculation of the size distribution.

3. Results and Discussion

3.1. Glass-Forming Ability and Intermetallic Phases of Cu-Mg-Ca Alloys

The ternary system Cu-Mg-Ca was previously shown to have GFA; various compositions were reported to form metallic glass by means of rapid quenching methods [34,35]. However, Ca and Mg can easily form oxides and nitrides, and they are highly reactive in the liquid state at high temperature. This makes the glass formation by rapid solidification of the melt a rather delicate process, and some experimental factors such as the atmosphere control, the material of the crucibles containing the melt and the thermal protocol during the melting and quenching have a big influence on the result. In this work we produced Cu-Mg-Ca rapidly solidified ribbons by melt spinning, Figure 1 shows the XRD patterns of all the compositions produced.

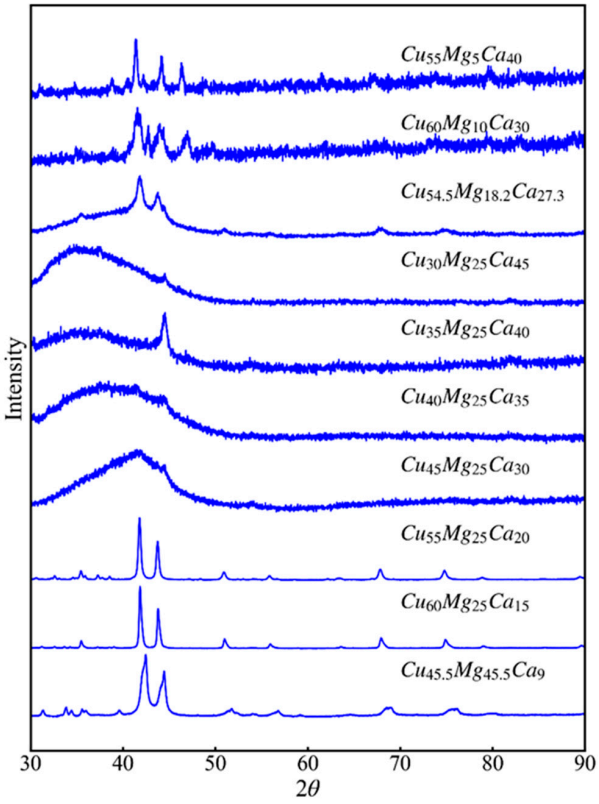

Figure 1. XRD spectra of the as-quenched ribbons of Cu-Mg-Ca alloys. The crystalline phases producing the Bragg reflections are discussed in the main text.

According to the XRD results, the set of produced materials can be classified in three series. Series 1 contains the alloys with the lowest Mg content ($Cu_{55}Mg_5Ca_{40}$, $Cu_{60}Mg_{10}Ca_{30}$, $Cu_{54.5}Mg_{18.2}Ca_{27.3}$). The as-quenched alloys of this series contain $CaCu_5$ crystallites (Hexagonal P6/mmm [36]) together with the amorphous phase. The fraction of amorphous phase obtained in series 1 increases with Mg content. Series 2 ($Cu_{30}Mg_{25}Ca_{45}$, $Cu_{35}Mg_{25}Ca_{40}$, $Cu_{40}Mg_{25}Ca_{35}$, $Cu_{45}Mg_{25}Ca_{30}$) are principally amorphous with a variable small fraction of crystalline phases; $CuMg_2$ (Orthorrombic Fddd [37]) is present in $Cu_{30}Mg_{25}Ca_{45}$ and it could also explain the principal crystalline reflection at $2\theta = 44.6°$ detected in the other materials of this series. However, the presence of small crystalline fractions of other intermetallic phases cannot be discarded. Finally, series 3 ($Cu_{55}Mg_{25}Ca_{20}$, $Cu_{60}Mg_{25}Ca_{15}$, $Cu_{45.5}Mg_{45.5}Ca_9$) contains the alloys with the lowest content of Ca. These alloys are basically composed by crystalline $MgCu_2$ (Cubic Fd-3m [38]) phase, which corresponds to the main nine Bragg reflections clearly shown in the $Cu_{60}Mg_{25}Ca_{15}$ spectrum, together with CaCu and Ca_2Cu phases which can explain the additional smaller diffraction peaks. The alloys of series 3 are completely crystalline.

Figure 2 shows the state (crystalline, partially crystalline or mainly amorphous) as function of the composition, the figure includes both the compositions characterized in this work as well as others we already reported in a previous publication [39]. All the alloys were produced by melt spinning. Figure 1 clearly shows the compositional dependence of the GFA. The high GFA region corresponds to copper contents between 25–60 at% and magnesium contents below 30 at%. In the case of the glass-forming compositions, the glass transition temperatures are found to be between 100 and 140 °C, as reported in reference [39]. The glassy alloys with lowest glass transition temperatures correspond to the ones with higher content of Mg. As detailed in the following subsections, only the compositions with significant amounts of amorphous phase were used for the study of the dealloying process.

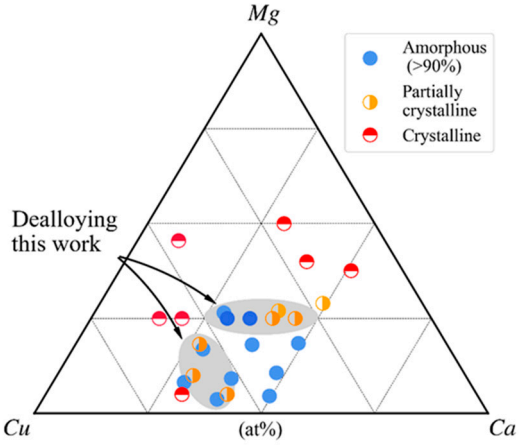

Figure 2. Glass-forming ability of the Cu-Mg-Ca system. All the alloys were obtained by rapid solidification in ribbon shape. Darker colors correspond to the alloys analyzed in this work and lighter color symbols to alloys already reported in reference [38].

3.2. *Dealloying of Series 2 in 0.04 M H_2SO_4*

The glassy or partially glassy Cu-Mg-Ca metals show a metallic silvery/golden shine (depending on the copper content) after production. However, they are extremely affected by corrosion. They corrode almost completely after a few months kept in ambient conditions becoming first blackish and finally crumbling. The low glass transition temperatures also imply low structural stability against aging and crystallization at room temperature. The low chemical and physical stability of this family of MG make them not appropriate for structural applications but, on the other hand, the easy corrosion can be advantageous for the generation of np-Cu by chemical etching. Production of np-Cu by dealloying Cu-Mg-Y amorphous alloys in a 0.04 M H_2SO_4 solution was reported in references [23,24,40]. We tested here a similar protocol in the case of the Cu-Mg-Ca alloys of series 2. Figure 3 shows the external aspect of the ribbons after chemical dealloying in 0.04 M H_2SO_4 for 30 min

until no bubbles emerged in the solution. The copper-like color and shine suggests that Mg and Ca elements were preferentially dissolved from the original alloys.

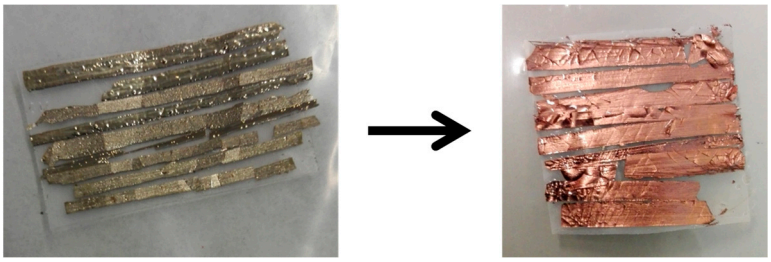

Figure 3. Examples of the external aspect of the Cu-Mg-Ca ribbons before and after chemical dealloying in 0.04 M H_2SO_4 for 30 min.

Figure 4 shows SEM micrographs of trenches cut on the surface of the dealloyed ribbons. Samples labelled as Cu45 ($Cu_{45}Mg_{25}Ca_{30}$) and Cu40 ($Cu_{40}Mg_{25}Ca_{35}$) show a nanoporous structure even in the most interior parts of the ribbons, implying that the dealloying process was able to reach the whole bulk of the materials. An image of the pristine structure of the Cu40 alloy is shown and described in the following subsection. On the other hand, in samples Cu35 ($Cu_{35}Mg_{25}Ca_{40}$) and Cu30 ($Cu_{30}Mg_{25}Ca_{45}$) the formation of the np-Cu structure is restricted to the first few microns below the surface. In all the samples many cracks appeared on both the surface and the bulk due to the stresses generated because of the volume change during dealloying (The smooth aspect of the outer surface of the ribbons seen in Figure 4 is due the protective Pt coating deposited during the digging of the trench by focus ion beam).

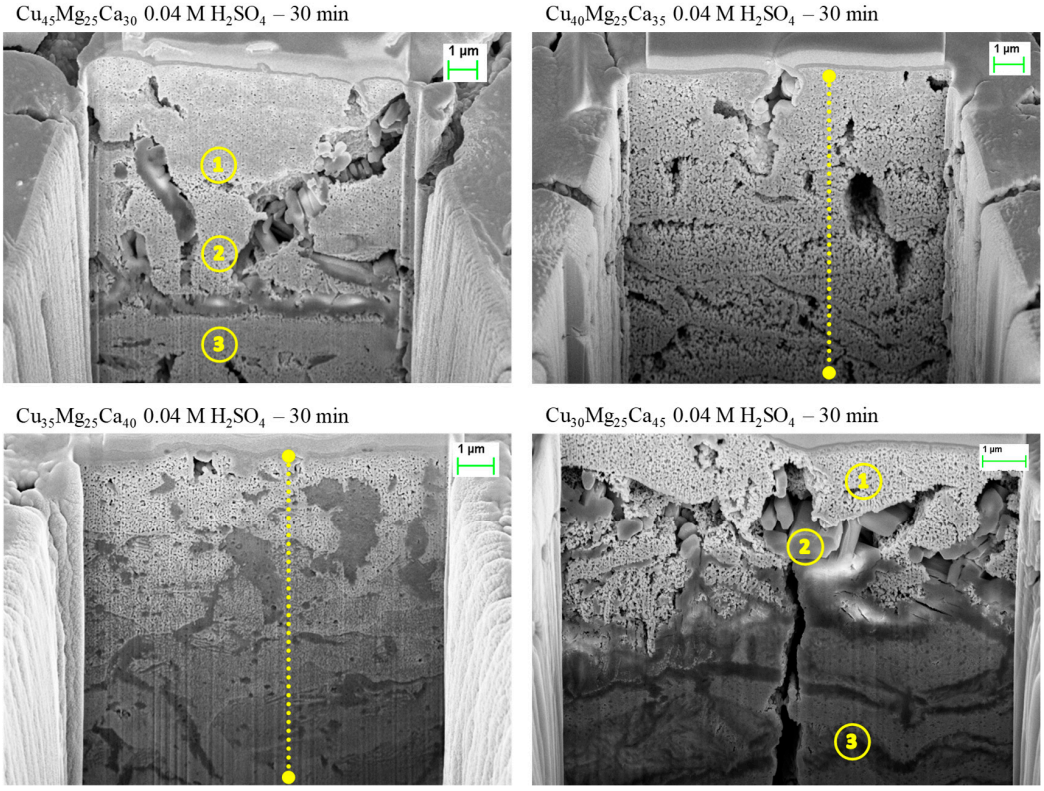

Figure 4. SEM images of the interior of dealloyed $Cu_{30}Mg_{25}Ca_{45}$, $Cu_{35}Mg_{25}Ca_{40}$, $Cu_{40}Mg_{25}Ca_{35}$ and $Cu_{45}Mg_{25}Ca_{30}$ ribbons. The yellow numbers and the dotted lines indicate the spots analyzed by EDS. The results of the composition analysis are displayed in Figure 5. XRD spectra of the as-quenched ribbons of Cu-Mg-Ca alloys. The crystalline phases producing the Bragg reflections are discussed in the main text.

Figure 5 shows the normalized content of Cu, Mg, Ca and S measured by EDS in the spots and lines highlighted with yellow color in Figure 4. The concentration is near 100 at% copper in Cu45 and Cu40 samples, even near the center of the ribbons. Therefore, the submersion in the sulfuric acid solution removed completely magnesium in all cases but calcium and sulfur contents remained significant in samples Cu35 and Cu30. In these two samples the presence of sulfur can be associated with a reaction between sulfuric acid and the precursor alloy elements leading to the precipitation of an S-containing phase, the identification of this phase will be discussed below. The results suggest that the formation of this phase competes with the dealloying process and hinders the progression of the np-Cu structure. As indicated by the EDS results, the reaction producing the S-containing phase seems to be prior or simultaneous to the formation of the np-Cu structure; in Cu35 and Cu30 samples the S-rich regions were found deep below the ribbon surface in zones where the np-Cu structure is scarcely present. In the zones nearer the surface, where the nanoporous structure is well formed, the S-containing crystallites detach from the nanoporous phase as seen in spot 2 of the right-bottom image (Cu30 alloy).

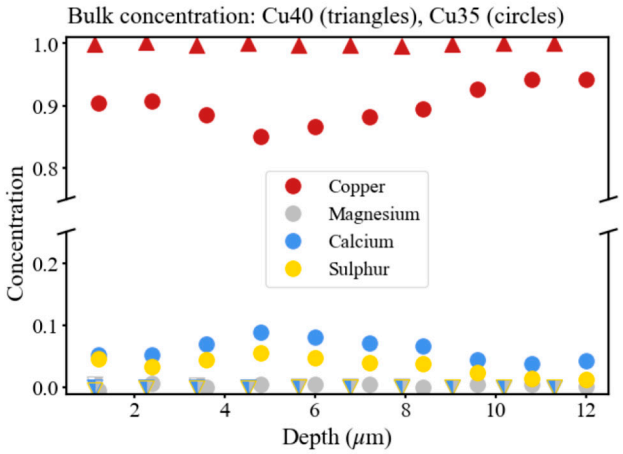

Cu45 (at%)	S	Ca	Mg	Cu
spot 1	0.6	0.8	0.0	98.7
spot 2	1.1	1.8	0.0	97.1
spot 3	0.5	0.7	0.0	98.7

Cu30 (at%)	S	Ca	Mg	Cu
spot 1	2.5	4.5	0.6	92.3
spot 2	8.8	17.3	0.5	73.3
spot 3	9.1	12.5	2.6	75.7

Figure 5. (**Left**) EDS concentrations obtained along the yellow lines in samples Cu40 and Cu35 after the submersion in 0.04 M H_2SO_4 for 30 min. (**Right**) Concentrations of the yellow spots in samples Cu45 and Cu30 after the submersion in 0.04 M H_2SO_4 for 30 min. (See Figure 4).

Figure 6 shows the XRD patterns of as-spun and dealloyed ribbons after immersion in the 0.04 M H_2SO_4 solution. The Cu45 and Cu40 spectra show the fcc-Cu peaks (indicated in the figure) together with small intensity reflections at lower angles. The large broadness of the fcc-Cu peaks is expected in nanoporous structures [40] and it is dependent on various factors such as the ligament size, the porous fraction, the microstrain of the lattice and the size of the copper crystallites forming the ligaments [41]. The contribution of additional phases increases in Cu35 and Cu30 in agreement with the SEM images above. The reflections observed at $2\theta = 31.2°$ and 34.1° can be attributed to Cu_7S_4 (monoclinic C2/m) phase, which is consistent with the presence of S-containing crystallites observed by SEM and EDS (The high-intensity peak at $2\theta \approx 70°$ observed in the XRD spectrum of the dealloyed Cu30 material is a spot coming from the Si monocrystal used as sample holder). The other peaks could not be properly identified and may be attributed to precipitates present only in the surface of the ribbons and not observed in the bulk. Here we should recall that some phases such as CaS and $CaSO_4$ have low solubility, the presence of small amounts of these phases cannot be discarded. It should be noted that the total area under the fcc-Cu peaks is very large compared to all the other observed reflections, confirming the almost complete dissolution of Ca and Mg as observed in SEM for samples Cu45 and Cu40.

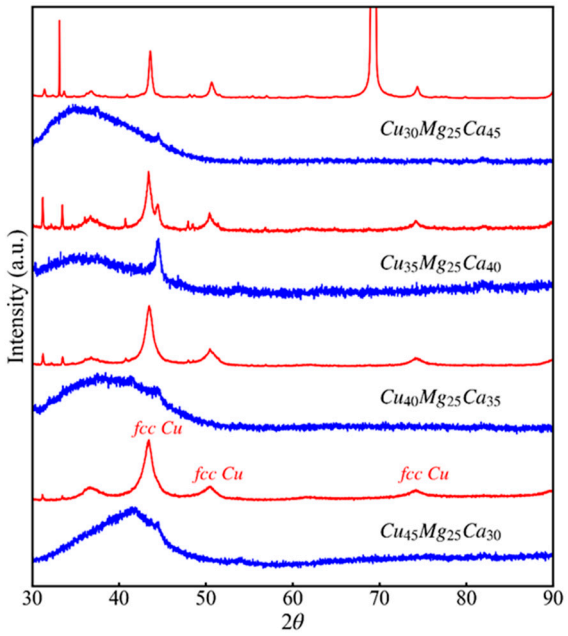

Figure 6. Comparison of XRD patterns of as-quenched (blue) and de-alloyed (red) $Cu_{30}Mg_{25}Ca_{45}$, $Cu_{35}Mg_{25}Ca_{40}$, $Cu_{40}Mg_{25}Ca_{35}$ and $Cu_{45}Mg_{25}Ca_{30}$ ribbons. The three peaks corresponding to the fcc copper structure are indicated in one of the spectra.

Figures 7 and 8 show the ligament and pore size distributions calculated from SEM images of the nanoporous structure in the region between the surface and ~5 μm depth. The average ligament sizes of the dealloyed Cu45, Cu40, Cu35 and Cu30 samples were estimated to be 195 ± 50, 190 ± 50, 155 ± 40 and 55 ± 20 nm, respectively, while the mean pore sizes are 60 ± 20, 65 ± 30, 75 ± 30 and 45 ± 20 nm. A survey of the results found in literature shows that np-Cu was obtained with mean ligament sizes of 60–80 nm for dealloyed $Mg_{60}Cu_{30}Y_{10}$ and 80–100 nm for $Mg_{50}Cu_{40}Y_{10}$, with nanopore size of 30–60 nm [24]. Similar nanoporous copper structures were also obtained in other works using other precursors [42–44].

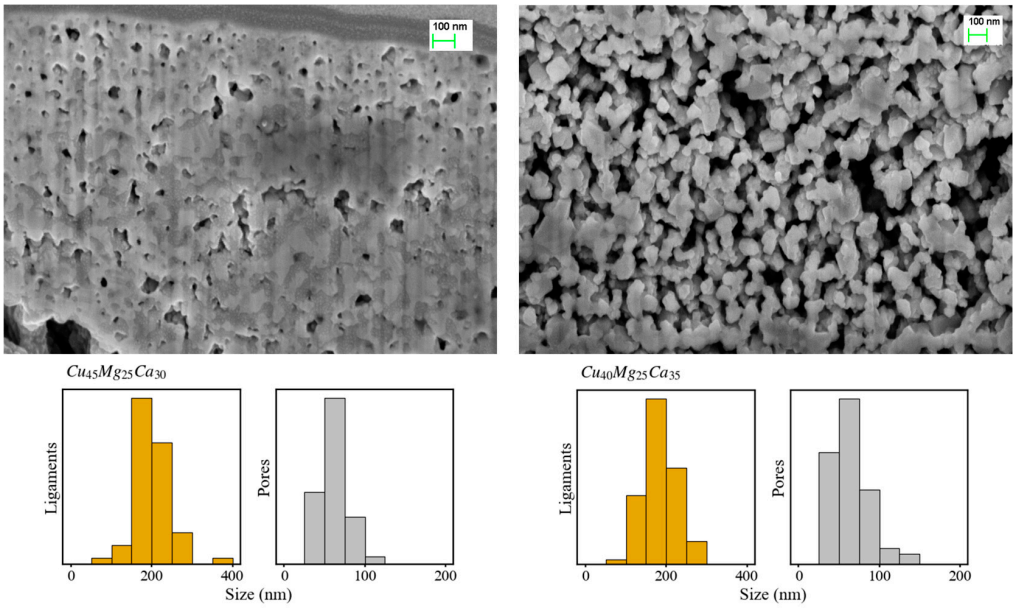

Figure 7. Images of the nanoporous copper structure formed near the surface of Cu45 (**left**) and Cu40 (**right**) samples. The corresponding size distributions of ligaments (orange) and ligaments (grey) are shown below.

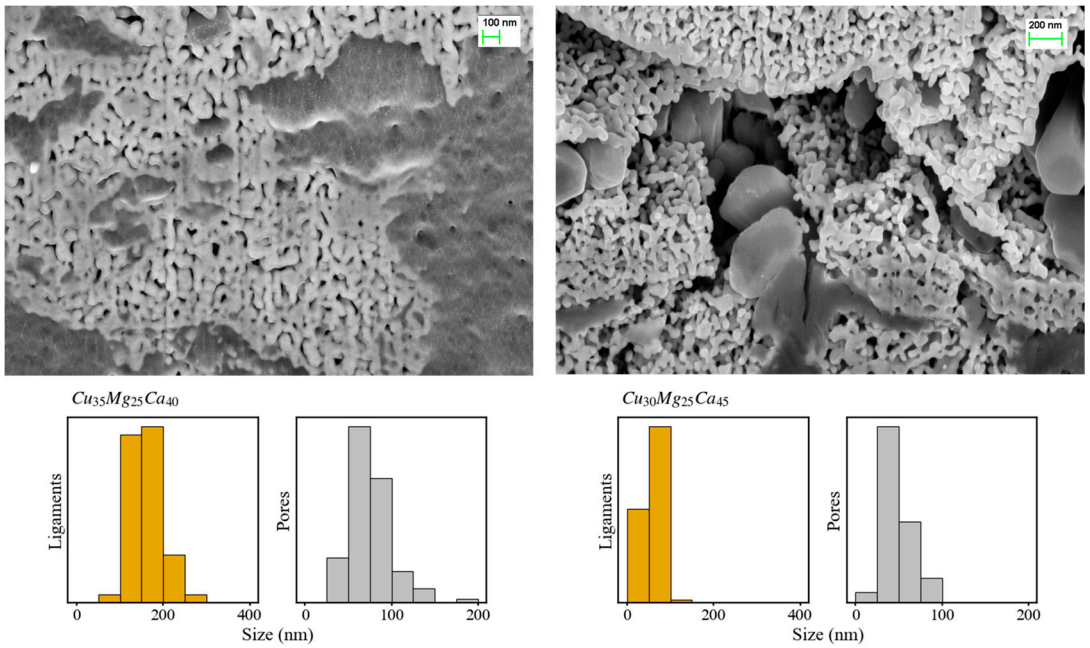

Figure 8. Images of the nanoporous copper structure formed near the surface of Cu35 (**left**) and Cu30 (**right**) samples. The corresponding size distributions of ligaments (orange) and ligaments (grey) are shown below.

Figure 9 presents the dependence of the ligament and pore size on the Cu content for the alloys of series 2. It is seen that the ligament size increases with the increase of the Cu content. The pore size also initially increases with Cu but reaches its maximum value at 35 at% Cu and then decreases. This indicates that, with the same dealloying time, the degree of coarsening of the copper ligaments is higher in the alloys with lower contents of the dissolving Mg and Ca elements, thus generating more compact np-Cu structures.

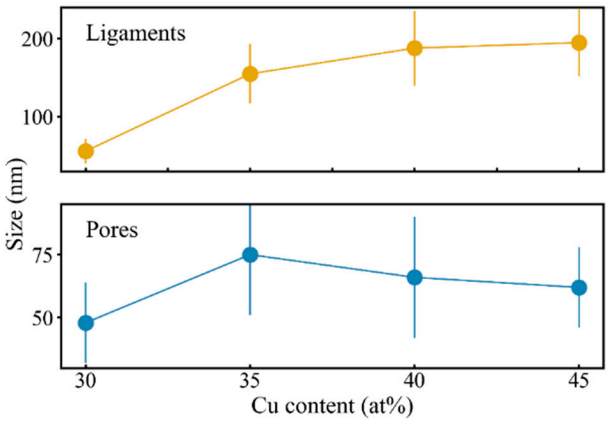

Figure 9. Average ligament and pore sizes as function of copper content for $Cu_{30}Mg_{25}Ca_{45}$, $Cu_{35}Mg_{25}Ca_{40}$, $Cu_{40}Mg_{25}Ca_{35}$, $Cu_{45}Mg_{25}Ca_{30}$ dealloyed in 0.04 M H_2SO_4.

In the present study, the remarkable electrode potential differences between Mg and Ca on one side (−2.37 V vs. standard hydrogen electrode (SHE) for Mg^+/Mg, −2.86 V for Ca^{2+}/Ca) and Cu on the other side (+0.34 V vs. SHE for Cu^{2+}/Cu) produces a high driving force for the dissolution of the less noble elements under free corrosion conditions [1,21,45]. This driving force leads to the selective dissolution of Mg and Ca atoms during the leaching process irrespective of the Cu content. As the dissolution of Cu can be ignored under free corrosion conditions [46–48], the formation and growth of

Cu clusters are mainly controlled by the surface diffusion of the nobler Cu atoms which construct the nanoporosity along the precursor/solution interface [2,16,49–51].

3.3. Dealloying in Distilled Water, 1 M HCl and 0.1 M NaOH Solutions

The fast dissolution of Mg and Ca observed in the sulfuric acid solution in the case of the alloys with higher amorphous content, encouraged us to investigate the dealloying process in other free corrosion conditions. The reactivity of Ca in water is very high, leading to violent spontaneous dissolution when submerged in water. Taken this into account we investigated the effect of submerging the Cu-Mg-Ca alloys in pure distilled water (PH = 7) as well as in 1 M HCl (pH = 3) and 0.1 M NaOH (pH = 10) solutions. A table with the samples produced, the various etching solutions and the immersion times examined in this work is shown in Supplementary Material Table S1. Figure 10 shows the results obtained for the case of $Cu_{40}Mg_{25}Ca_{35}$ (Cu40) alloy which, as already detailed above, was totally dealloyed by immersion in 0.04 M H_2SO_4. Figure 10 also shows the initial state of the alloy, which contains metallic glassy phase together with small spherical crystalline precipitates. This initial state was found similar in all the alloys of series 2 for which XRD shows small crystalline reflections in addition to the amorphous halo (see Figure 1).

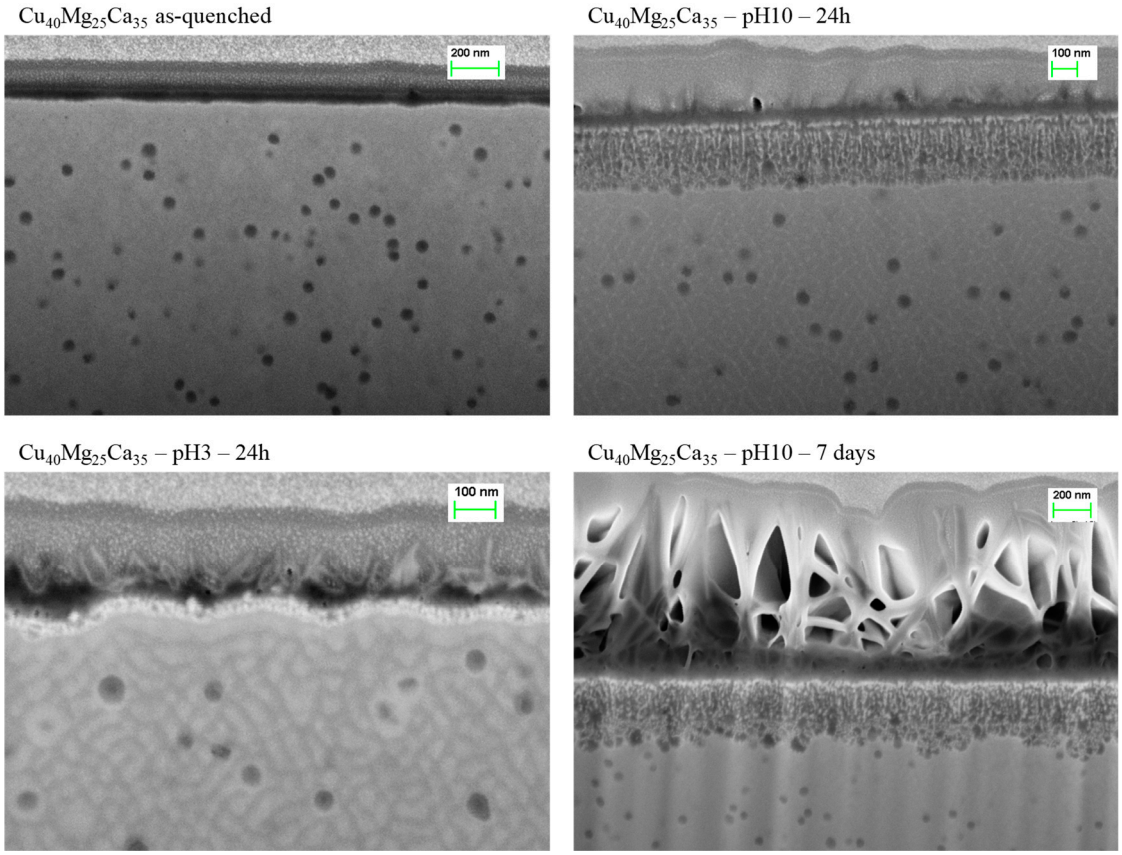

Figure 10. SEM images of transversal cuts of $Cu_{40}Mg_{25}Ca_{35}$ in the initial state (**left-top**) and dealloyed by immersion in pH = 3 and pH = 10 solutions.

In the case of Cu40, as seen in Figure 10, after 24 h in pH3 and pH7 media, the corrosion process generates an extremely thin porous layer of less than 50 nm depth. On the other hand, the immersion in the pH10 solution generates a 200 nm porous layer. In all cases the dealloyed layer has an extremely fine structure compared to the np-Cu structures obtained in the sulfuric acid solution, as if the dissolution process was stopped before the coarsening of the ligaments which is expected to proceed with dealloying time [15]. As seen in Figure 10 (bottom-right image) the extension of the treatment during several days increases the layer of outer precipitates but it does not increase the

depth of the dealloyed region. The results obtained for the other alloys of series 2, not shown here, are qualitatively similar, although the complete study of the effect of the different leaching solutions was only performed for Cu40. Therefore, for the alloys of series 2 immersed in the pH = 3, pH = 7 and pH = 10 solutions, the formation of precipitates on the surface seems to protect them from further dissolution of the Mg and Ca located in the inner regions of the material. The formation of these outer precipitates was not observed for the dealloying process when using the sulfuric acid solution.

Finally, the partially crystalline alloys of series 1 ($Cu_{55}Mg_5Ca_{40}$, $Cu_{60}Mg_{10}Ca_{30}$, $Cu_{54.5}Mg_{18.2}Ca_{27.3}$) were also exposed to dealloying in the pH = 3, pH = 7 and pH = 10 media. As described above, this series of alloys have an initial microstructure basically made of amorphous phase and $CaCu_5$ crystals. Although these alloys contain a significant fraction of crystalline intermetallic phase, we tested the dealloying process of series 1 in the different solutions to better assess the effects of the alloy composition and microstructure on the dealloying behavior. As seen in Figure 11, the crystalline $CaCu_5$ phase is not dissolved while the amorphous fraction is significantly attacked. For instance, in the case of $Cu_{55}Mg_5Ca_{40}$ the inter-crystallite amorphous phase was completely dealloyed in the whole interior of the material by immersion in the pH = 10 solution (Figure 11 left-bottom image). The same process was observed in pure water (Figure 11 left-top image), although the extend in depth of the corroded region was not checked. Also, a similar process was observed in $Cu_{60}Mg_{10}Ca_{30}$, with a final partially dealloyed structure dependent on the initial microstructure. On the other hand, in the case of $Cu_{54.5}Mg_{18.2}Ca_{27.3}$, the results were similar to the ones obtained for series 2, with the generation of only superficial porosity and the development of a thick precipitate layer on top of the ribbons. In all cases, however, the pH = 10 solution provided the higher degree of dealloying compared to pH = 3 and pure water. At present, we do not have any clue of the chemical mechanisms that may be responsible for this behavior.

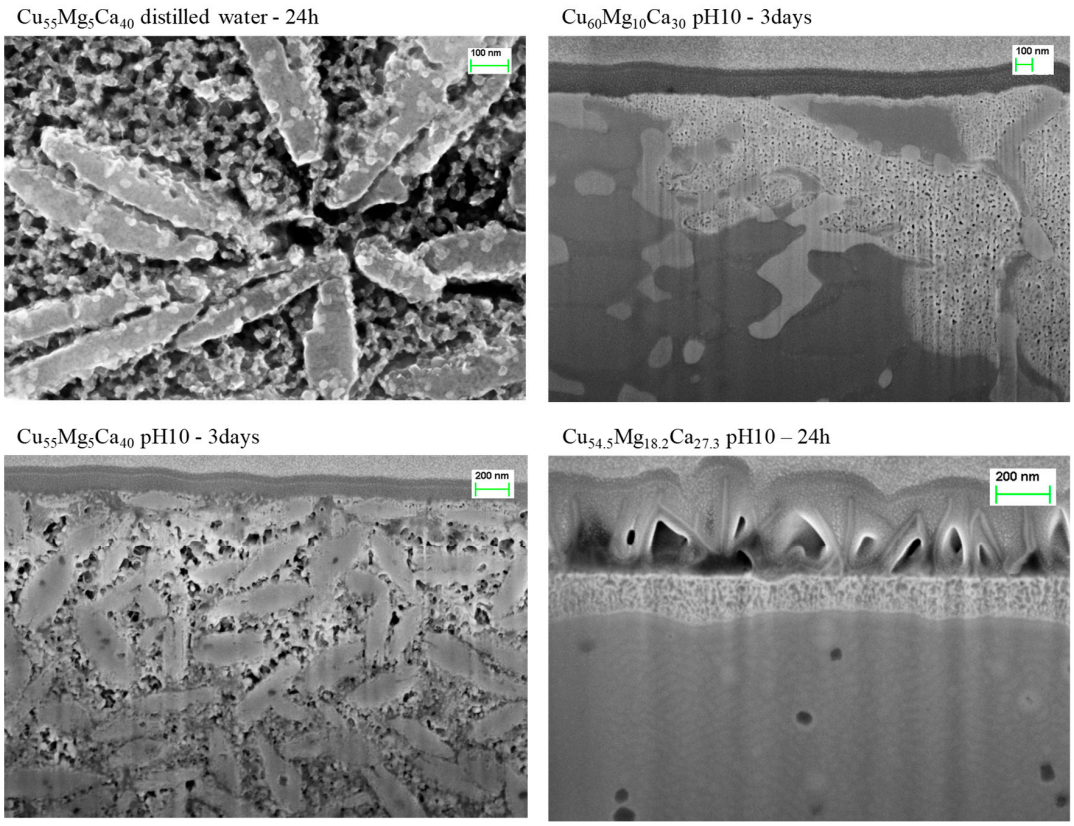

Figure 11. Selected SEM images of the surface (**left-top**) and of transversal cuts (**rest of images**) of $Cu_{55}Mg_5Ca_{40}$, $Cu_{60}Mg_{10}Ca_{30}$, $Cu_{54.5}Mg_{18.2}Ca_{27.3}$ dealloyed by immersion in pure water and pH = 10 solution.

It is worth noting that although the crystalline phase present in the alloys of series 1 inhibits the formation of a continuous np-Cu structure, on the other hand diminishes the probability of crack formation. This is due to the less quantity of total material dissolved which consequently reduces the generation of stresses in the material during the dealloying process. It is also interesting to note that while the pH = 10 solution is only able to dealloy the surface of the materials containing higher Mg content (series 2 and $Cu_{54.5}Mg_{18.2}Ca_{27.3}$ of series 1), it is able to attack the inner regions in the case of $Cu_{55}Mg_5Ca_{40}$ and $Cu_{60}Mg_{10}Ca_{30}$ although only the non-crystalline domains. It seems that the less quantity of dissolved Mg and Ca, the latter fixed in the $CaCu_5$ crystalline phase, avoids the formation of the thick protective precipitate layer. This suggests that the dealloying of Cu-Mg-Ca precursors in an electrochemical cell, with dissolution rates of Ca and Mg controlled by the applied potential, would allow a major control of the process and it would be possible to obtain the formation of np-Cu structures in solutions of very low concentration or even directly in pure water. These results are also important for understanding the free corrosion behavior expected for the Cu-Mg-Ca biocompatible alloys.

4. Conclusions

Cu-Mg-Ca alloys were produced in ribbon shape by melt spinning. The characterization of the alloys provided new information on the region within the ternary diagram where there is the highest GFA, and which are the competing crystalline phases. The formation of continuous nanoporous copper structures was obtained by dealloying the materials with the higher fraction of amorphous phase in a sulfuric acid solution. For some compositions Ca and Mg were totally depleted obtaining a pure fcc copper porous structure. The change in composition was observed to be one of the factors controlling the ligament and porous sizes and, consequently, the compactness of the nanoporous network. Contrary to the sulfuric acid solution, only superficial dealloying was obtained by immersion of the amorphous metals in HCl and NaOH solutions as well as in pure water. Finally, dealloying of compositions with lower Mg contents was observed to produce nanoporous/crystal microstructures when dealloying in water and NaOH solutions. The results presented in this work show the different corrosion behaviors of the biocompatible Cu-Mg-Ca alloys depending on their initial composition and microstructure. It is shown that these alloys are good candidates to be used as precursors for new nanoporous materials, due to the easy dissolution of Mg and Ca as well as to the wide range of amorphous and partially crystalline microstructures that can be obtained by applying different solidification protocols.

Supplementary Materials: The following are available online at http://www.mdpi.com/2075-4701/8/11/919/s1.

Author Contributions: W.B.M. performed the most part of the experimental work and posterior characterization. E.P. and J.J.S were directly supervising the work and the analysis. L.E. and M.K. participated in discussion and analysis of the results. All authors contributed to conceptualization and writing.

Funding: E.P. acknowledges financial support from MINECO (grant FIS2017-82625-P) and Generalitat de Catalunya (grant 2017SGR0042).

Acknowledgments: We acknowledge the priceless help of Trifon Trifonov at the Centre de Recerca en Ciència i Enginyeria Multiescala de Barcelona.

Conflicts of Interest: The authors declare no conflict of interest. The funders had no role in the design of the study; in the collection, analyses, or interpretation of data; in the writing of the manuscript, or in the decision to publish the results.

References and Note

1. Erlebacher, J.; Aziz, M.J.; Karma, A.; Dimitrov, N.; Sieradzki, K. Evolution of nanoporosity in dealloying. *Nature* **2001**, *410*, 450–453. [CrossRef] [PubMed]
2. Erlebacher, J. An Atomistic Description of Dealloying. *J. Electrochem. Soc.* **2004**, *151*, C614. [CrossRef]
3. Bond, G.C.; Thompson, D.T. Catalysis by Gold. *Catal. Rev.* **1999**, *41*, 319–388. [CrossRef]

4. Chen, L.Y.; Yu, J.S.; Fujita, T.; Chen, M.W. Nanoporous copper with tunable nanoporosity for SERS applications. *Adv. Funct. Mater.* **2009**, *19*, 1221–1226. [CrossRef]
5. Ding, Y.; Chen, M. Nanoporous Metals for Catalytic and Optical Applications. *MRS Bull.* **2009**, *34*, 569–576. [CrossRef]
6. Hakamada, M.; Nakano, H.; Furukawa, T.; Takahashi, M.; Mabuchi, M. Hydrogen storage properties of nanoporous palladium fabricated by dealloying. *J. Phys. Chem. C* **2010**, *114*, 868–873. [CrossRef]
7. Pikul, J.H.; Zhang, G.H.; Cho, J.; Braun, P.V.; King, W.P. High-power lithium ion microbatteries from interdigitated three-dimensional bicontinuous nanoporous electrodes. *Nat. Commun.* **2013**, *4*, 1732. [CrossRef] [PubMed]
8. Kramer, D.; Viswanath, R.N.; Weissmüller, J. Surface-Stress Induced Macroscopic Bending of Nanoporous Gold Cantilevers. *Nano Lett.* **2004**, *4*, 793–796. [CrossRef]
9. Mangipudi, K.R.; Epler, E.; Volkert, C.A. Morphological similarity and structure-dependent scaling laws of nanoporous gold from different synthesis methods. *Acta Mater.* **2017**, *140*, 337–343. [CrossRef]
10. Xue, Y.; Markmann, J.; Duan, H.; Weissmüller, J.; Huber, P. Switchable imbibition in nanoporous gold. *Nat. Commun.* **2014**, *5*, 4237. [CrossRef] [PubMed]
11. Masuda, H.; Fukuda, K. Ordered Metal Nanohole Arrays Made by a Two-Step Replication of Honeycomb Structures of Anodic Alumina. *Science* **1995**, *268*, 1466–1468. [CrossRef] [PubMed]
12. Wadley, H.N.G. Cellular Metals Manufacturing. *Adv. Eng. Mater.* **2002**, *4*, 726–733. [CrossRef]
13. Zhang, Z.; Wang, Y.; Qi, Z.; Zhang, W.; Qin, J.; Frenzel, J. Generalized fabrication of nanoporous metals (Au, Pd, Pt, Ag, and Cu) through chemical dealloying. *J. Phys. Chem. C* **2009**, *113*, 12629–12636. [CrossRef]
14. Pugh, D.V.; Dursun, A.; Corcoran, S.G. Electrochemical and Morphological Characterization of Pt–Cu Dealloying. *J. Electrochem. Soc.* **2005**, *152*, B455. [CrossRef]
15. Qian, L.H.; Chen, M.W. Ultrafine nanoporous gold by low-temperature dealloying and kinetics of nanopore formation. *Appl. Phys. Lett.* **2007**, *91*, 2005–2008. [CrossRef]
16. Snyder, J.; Asanithi, P.; Dalton, A.B.; Erlebacher, J. Stabilized nanoporous metals by dealloying ternary alloy precursors. *Adv. Mater.* **2008**, *20*, 4883–4886. [CrossRef]
17. Smith, A.J.; Trimm, D.L. The Preparation of Skeletal Catalysts. *Annu. Rev. Mater. Res.* **2005**, *35*, 127–142. [CrossRef]
18. Min, U.-S.; Li, J.C.M. The microstructure and dealloying kinetics of a Cu-Mn alloy. *J. Mater. Res.* **1994**, *9*, 2878–2883. [CrossRef]
19. Lu, H.B.; Li, Y.; Wang, F.H. Synthesis of porous copper from nanocrystalline two-phase Cu-Zr film by dealloying. *Scr. Mater.* **2007**, *56*, 165–168. [CrossRef]
20. Liu, W.; Zhang, S.; Li, N.; Zheng, J.; An, S.; Xing, Y. Monolithic Nanoporous Copper ribbons from Mg-Cu Alloys with Copper Contents below 33 at.%: Fabrication, Structure Evolution and Coarsening Behavior along the Thickness Direction. *Int. J. Electrochem. Sci.* **2011**, *6*, 5445–5461.
21. Yu, J.; Ding, Y.; Xu, C.; Inoue, A.; Sakurai, T.; Chen, M. Nanoporous Metals by Dealloying Multicomponent Metallic Glasses. *Chem. Mater.* **2008**, *20*, 4548–4550. [CrossRef]
22. Lang, X.Y.; Guo, H.; Chen, L.Y.; Kudo, A.; Yu, J.S.; Zhang, W.; Inoue, A.; Chen, M.W. Novel Nanoporous Au−Pd Alloy with High Catalytic Activity and Excellent Electrochemical Stability. *J. Phys. Chem. C* **2010**, *114*, 2600–2603. [CrossRef]
23. Luo, X.; Li, R.; Liu, Z.; Huang, L.; Shi, M.; Xu, T.; Zhang, T. Three-dimensional nanoporous copper with high surface area by dealloying Mg–Cu–Y metallic glasses. *Mater. Lett.* **2012**, *76*, 96–99. [CrossRef]
24. Luo, X.; Li, R.; Huang, L.; Zhang, T. Nucleation and growth of nanoporous copper ligaments during electrochemical dealloying of Mg-based metallic glasses. *Corros. Sci.* **2013**, *67*, 100–108. [CrossRef]
25. Jin, Y.; Li, R.; Zhang, T. Formation of nanoporous silver by dealloying Ca-Ag metallic glasses in water. *Intermetallics* **2015**, *67*, 166–170. [CrossRef]
26. St.Amand, R.; Giessen, B.C. Easy glass formation in simple metal alloys: Amorphous metals containing calcium and strontium. *Scr. Metall.* **1978**, *12*, 1021–1026. [CrossRef]
27. De Tendler, R.H.; Kovacs, J.A.; Alonso, J.A. Theoretical calculation of the amorphous alloy range of the Mg-Cu system. *J. Mater. Sci.* **1992**, *27*, 4935–4939. [CrossRef]
28. Inoue, A.; Masumoto, T. Mg-based amorphous alloys. *Mater. Sci. Eng. A* **1993**, *173*, 1–8. [CrossRef]

29. Somoza, J.A.; Gallego, L.J.; Rey, C.; Rozenberg, S.; Arcondo, B.; Sirkin, H.; De Tendler, R.H.; Kovacs, J.A.; Alonso, J.A. An experimental and theoretical study of the glass-forming region of the Mg-Cu-Sn system. *J. Mater. Sci.* **1995**, *30*, 40–46. [CrossRef]
30. Li, R.; Liu, X.J.; Wang, H.; Wu, Y.; Chu, X.M.; Lu, Z.P. Nanoporous silver with tunable pore characteristics and superior surface enhanced Raman scattering. *Corros. Sci.* **2014**, *84*, 159–164. [CrossRef]
31. Li, R.; Liu, X.J.; Wang, H.; Zhou, D.Q.; Wu, Y.; Lu, Z.P. Formation mechanism and characterization of nanoporous silver with tunable porosity and promising capacitive performance by chemical dealloying of glassy precursor. *Acta Mater.* **2016**, *105*, 367–377. [CrossRef]
32. Senkov, O.N.; Miracle, D.B.; Keppens, V.; Liaw, P.K. Development and Characterization of Low-Density Ca-Based Bulk Metallic Glasses: An Overview. *Metall. Mater. Trans. A* **2007**, *39*, 1888–1900. [CrossRef]
33. Li, H.F.; Zheng, Y.F. Recent advances in bulk metallic glasses for biomedical applications. *Acta Biomater.* **2016**, *36*, 1–20. [CrossRef] [PubMed]
34. Senkov, O.N.; Scott, J.M. Specific criteria for selection of alloy compositions for bulk metallic glasses. *Scr. Mater.* **2004**, *50*, 449–452. [CrossRef]
35. Senkov, O.N.; Scott, J.M.; Miracle, D.B. Composition range and glass forming ability of ternary Ca-Mg-Cu bulk metallic glasses. *J. Alloys Compd.* **2006**, *424*, 394–399. [CrossRef]
36. Smith, D. Penn State University, University Park, PA, USA. ICDD Grant-in-Aid, 1973.
37. Hanawalt, J.D.; Rinn, H.W.; Frevel, L.K. Chemical analysis by x-ray diffraction-Classification and use of x-ray diffraction patterns. *Ind. Eng. Chem. Ed.* **1938**, *10*, 457–512. [CrossRef]
38. Ohba, T.; Kitano, Y.; Komura, Y. The Charge-Density Study of the Laves Phases, $MgZn_2$ and $MgCu_2$. *Acta Crystallogr. Sect. C-CRYSTAL Struct. Commun.* **1984**, *40*, 1–5. [CrossRef]
39. Zhang, Y.; Greer, A.L.; Pineda, E. Fragility and glass-forming ability of the Ca–Mg–Cu system. *J. Alloys Compd.* **2007**, *434–435*, 145–148.
40. Luo, X.; Li, R.; Zong, J.; Zhang, Y.; Li, H.; Zhang, T. Enhanced degradation of azo dye by nanoporous-copper-decorated Mg–Cu–Y metallic glass powder through dealloying pretreatment. *Appl. Surf. Sci.* **2014**, *305*, 314–320. [CrossRef]
41. Graf, M.; Ngô, B.-N.D.; Weissmüller, J.; Markmann, J. X-ray studies of nanoporous gold: Powder diffraction by large crystals with small holes. *Phys. Rev. Mater.* **2017**, *1*. [CrossRef]
42. Dan, Z.; Qin, F.; Yamaura, S.; Xie, G.; Makino, A.; Hara, N. Refinement of Nanoporous Copper by Dealloying MgCuY Amorphous Alloys in Sulfuric Acids Containing Polyvinylpyrrolidone. *J. Electrochem. Soc.* **2014**, *161*, C120–C125. [CrossRef]
43. Dan, Z.; Qin, F.; Sugawara, Y.; Muto, I.; Hara, N. Fabrication of nanoporous copper by dealloying amorphous binary Ti-Cu alloys in hydrofluoric acid solutions. *Intermetallics* **2012**, *29*, 14–20. [CrossRef]
44. Dan, Z.; Qin, F.; Makino, A.; Sugawara, Y.; Muto, I.; Hara, N. Fabrication of nanoporous copper by dealloying of amorphous Ti-Cu-Ag alloys. *J. Alloys Compd.* **2014**, *586*, S134–S138. [CrossRef]
45. Ding, Y.; Kim, Y.-J.; Erlebacher, J. Nanoporous Gold Leaf: "Ancient Technology"/Advanced Material. *Adv. Mater.* **2004**, *16*, 1897–1900. [CrossRef]
46. Pickering, H.W.; Wagner, C. Electrolytic Dissolution of Binary Alloys Containing a Noble Metal. *J. Electrochem. Soc.* **1967**, *114*, 698–706. [CrossRef]
47. Moreira, A.H.; Benedetti, A.V.; Cabot, P.L.; Sumodjo, P.T.A. Electrochemical behaviour of copper electrode in concentrated sulfuric acid solutions. *Electrochim. Acta* **1993**, *38*, 981–987. [CrossRef]
48. Ma, H.; Chen, S.; Yin, B.; Zhao, S.; Liu, X. Impedance spectroscopic study of corrosion inhibition of copper by surfactants in the acidic solutions. *Corros. Sci.* **2003**, *45*, 867–882. [CrossRef]
49. Smith, A.J.; Tran, T.; Wainwright, M.S. Kinetics and mechanism of the preparation of Raney® copper. *J. Appl. Electrochem.* **1999**, *29*, 1085–1094. [CrossRef]
50. Parida, S.; Kramer, D.; Volkert, C.A.; Rösner, H.; Erlebacher, J.; Weissmüller, J. Volume change during the formation of nanoporous gold by dealloying. *Phys. Rev. Lett.* **2006**, *97*, 4–7. [CrossRef] [PubMed]
51. Aburada, T.; Fitz-Gerald, J.M.; Scully, J.R. Synthesis of nanoporous copper by dealloying of Al-Cu-Mg amorphous alloys in acidic solution: The effect of nickel. *Corros. Sci.* **2011**, *53*, 1627–1632. [CrossRef]